Exchange Coupling in Soft Magnetic Nanostructures and Its Direct Effect on Their Theranostic Properties

Vikas Nandwana,[#,¶] Ruiying Zhou,[#,¶] Jeotikanta Mohapatra,[§] Sungkyu Kim,[#,¶] Pottumarthi V. Prasad,[†] J. P. Liu,[§] and Vinayak P. Dravid*,[#,¶]

[#]Department of Materials Science & Engineering, Northwestern University, Evanston, Illinois 60208, United States
[¶]International Institute of Nanotechnology, Evanston, Illinois 60208, United States
[§]Department of Physics, The University of Texas at Arlington, Arlington, Texas 76019, United States
[†]Department of Radiology, Northshore University Healthcare, Evanston, Illinois 60201, United States

S Supporting Information

ABSTRACT: Exchange coupling between hard and soft magnetic materials at the nanoscale exhibits novel or improved physical properties for energy and data storage applications. Recently, exchange coupling has also been explored in core/shell magnetic nanostructures (MNS) composed of hard and soft magnetic spinel ferrites, but applications have been limited in biomedicine due to the presence of "toxic" cobalt based ferrites as hard magnetic component. We report core/shell MNS where both core and shell components are soft magnetic ferrites (Fe_3O_4, $MnFe_2O_4$, and $Zn_{0.2}Mn_{0.8}Fe_2O_4$) and show that exchange coupling still exists due to the difference in their anisotropy. The physical properties (saturation magnetization, susceptibility, anisotropy, r_2 relaxivity, and specific absorption rate) of core/shell MNS are compared with the same size single phase counterparts which excludes any size dependent effect and gives the direct effect of exchange coupling. After optimization of core and shell components and their proportions, we have shown that a core/shell MNS shows significantly higher contrast enhancement and thermal activation properties than their single phase counterparts due to exchange coupling between core and shell ferrites. Our finding provides a novel way to improve theranostic properties of spinel ferrite based MNS while maintaining their biocompatibility.

KEYWORDS: magnetic nanostructures, exchange coupling, contrast enhancement, thermal activation, theranostics
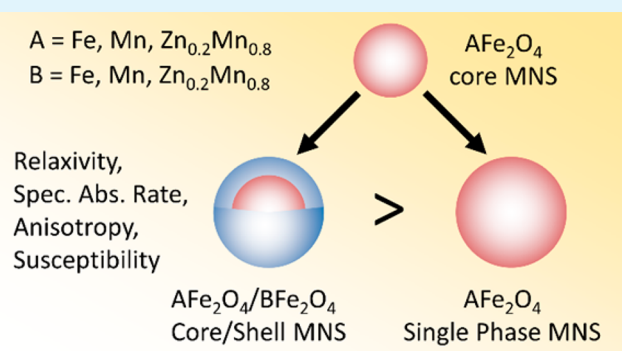
INTRODUCTION

Interfacial exchange coupling between hard magnetic (high anisotropy) and soft magnetic (low anisotropy) nanomaterials exhibits novel or improved physical properties.[1,2] The exchange coupling can be optimized through the control of the nanostructure and the exchange interactions. Hence, this phenomenon has been exploited in thin films, intermixing of nanoparticles, heterostructures, and core/shell nanostructures.[3−8] Core/shell nanostructures demonstrate the most effective exchange coupling due to the maximum interfacial exchange interactions between hard and soft magnetic phases.[4,6] Moreover, the physical properties of the exchange-coupled core/shell nanostructures can be tuned by controlling the proportion and dimension of the core and/or shell material. Exchange-coupled core/shell nanostructures have shown excellent applications in permanent magnets, recording media, and microwave absorption.[4,5,9−13] Exchange interactions between antiferromagnetic and ferromagnetic materials generate exchange bias and enhanced anisotropy that can overcome the superparamagnetic limit which makes it important for recording media applications.[12,13] Exchange coupling between soft and hard ferromagnetic materials demonstrates higher energy product which is desired in permanent magnets applications.[4,5] Exchange-coupled hard/soft nanocomposites have shown enhanced microwave absorption (reflection loss) to attenuate unwanted electromagnetic signals in devices working at microwave and higher frequencies.[9−11]

Recently, exchange coupling has been explored to modulate the physical properties of superparamagnetic spinel ferrite based magnetic nanostructures (MNS).[14,15] The spinel ferrite based MNS have shown significant importance in biomedical applications due to their ability to enhance contrast in magnetic resonance imaging (MRI) and thermal activation properties under radio frequency (RF) field.[16−21] While the enhanced localized MRI contrast can be utilized for

diagnostics, the thermal activation capability can be employed for thermal/chemo/biotherapy. Seshadri and co-workers demonstrated that saturation magnetization, coercivity, and blocking temperature of the $CoFe_2O_4$ nanoparticles can be tuned by coating $ZnFe_2O_4$ shell (or vice versa) due to exchange coupling between $CoFe_2O_4$ and $ZnFe_2O_4$.[22] Cheon and co-workers showed the specific absorption rate (SAR) of 9 nm $CoFe_2O_4$ can be increased significantly when coated with a 3 nm shell of $MnFe_2O_4$.[14] They reported the SAR of 9 nm $CoFe_2O_4$, 15 nm $MnFe_2O_4$, and 15 nm $CoFe_2O_4/MnFe_2O_4$ to be 415, 411, and 2280 W/g, respectively.[14] Song and Zhang showed that the coercivity and blocking temperature of $CoFe_2O_4$ nanoparticles can be tuned by coating different shell thicknesses of $MnFe_2O_4$ (or vice versa).[15] In all these studies, $CoFe_2O_4$ was chosen as the hard magnetic material due to its high magnetocrystalline anisotropy ($K_u > 10^5$ J/m^3) while $ZnFe_2O_4$ and $MnFe_2O_4$ were chosen as soft magnetic material.[14,15,23] However, it should be noted that all these physical properties (saturation magnetization, anisotropy, blocking temperature, and SAR) of MNS also depend on their size. Hence, when the physical properties of core/shell nanostructure are compared with core nanoparticles, the change observed is not only due to exchange coupling but also due to size. For example, it would be difficult to compare 8 nm $CoFe_2O_4$ with 8 nm/2 nm $CoFe_2O_4/MnFe_2O_4$ core/shell MNS since the 12 nm core/shell MNS will always show different physical properties than 8 nm core MNS. However, 12 nm $CoFe_2O_4$ MNS can be considered as 8 nm/2 nm $CoFe_2O_4/CoFe_2O_4$ core/shell MNS and can be compared with 8 nm/2 nm $CoFe_2O_4/MnFe_2O_4$ core/shell MNS.

Hence, to observe the true effect of exchange coupling, it is critical to keep the size of MNS constant during the comparison of single phase and core/shell MNS. To the best of our knowledge, none of the previous reports show such comparison. In addition, recent reports suggest that $CoFe_2O_4$ nanoparticles, that are used as the "hard magnetic" component in the above reports, can induce oxidative stress and cytotoxicity and hence are not considered biocompatible for biomedical applications.[24−29]

Here, we report exchange-coupled core/shell MNS composed of spinel ferrites that address both of these issues (biocompatibility and size effect). Fe_3O_4, $MnFe_2O_4$, and $Zn_{0.2}Mn_{0.8}Fe_2O_4$ have been chosen as core and/or shell MNS components due to their biocompatibility in addition to high contrast enhancement and thermal activation properties (Figure 1).[30] Physical properties of core/shell MNS are compared with same size core or shell components (single phase MNS). Unlike previous reports, such comparison avoids any size dependent effect and gives the direct effect of exchange coupling.[14,15,22] Although all these ferrites are considered soft magnetic due to lower anisotropy ($K_u \sim 10^3$ J/m^3), using magnetic characterization, we have shown the exchange interactions between core and shell components can still occur due to the difference in their anisotropy. As a result, we have observed higher susceptibility and anisotropy of core/shell MNS compared to same size single phase MNS. Using relaxation and thermal activation plots, we have shown that the increase in susceptibility and anisotropy significantly improves contrast enhancement and thermal activation properties of core/shell MNS compared to same size single phase MNS. We also show that the enhanced theranostic properties of MNS can be further tuned by choosing the right core and shell components and their dimensions. Overall, our finding
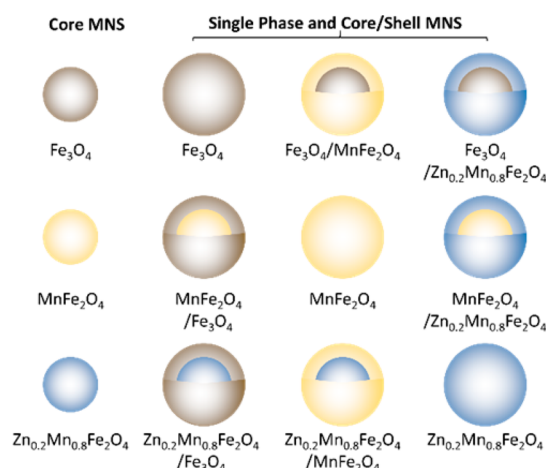

Figure 1. Library of core/shell and single phase MNS using three different ferrite core MNS.

confirms the exchange coupling in soft and biocompatible MNS and presents an alternative way to modulate theranostic properties of MNS for biomedical applications.

EXPERIMENTAL DETAILS

Synthesis of Single Phase and Core/Shell Magnetic Nanostructures. The 8 nm Fe_3O_4, $MnFe_2O_4$, and $Zn_{0.2}Mn_{0.8}Fe_2O_4$ nanoparticles were synthesized using previously reported thermal decomposition methods.[30,31] Core/shell nanostructures were synthesized by the seed mediated approach for synthesis where the 8 nm MFe_2O_4 (M = Fe, Mn, $Zn_{0.2}Mn_{0.8}$) nanoparticles were used as seeds (labeled as core MNS) to grow shell of the same or different material. For example, when Fe_3O_4 core MNS were used as seeds, addition of Mn and Mn+Zn precursor resulted in $Fe_3O_4/MnFe_2O_4$ and $Fe_3O_4/Zn_{0.2}Mn_{0.8}Fe_2O_4$ (labeled as core/shell MNS), respectively, while addition of Fe precursor results in larger size Fe_3O_4 (labeled as single phase MNS). A library of core/shell nanostructures was synthesized by combination of these three ferrites as core and shell components. In a typical $Fe_3O_4/MnFe_2O_4$ nanostructure synthesis, Fe_3O_4 NPs (25 mg as core NPs), $Fe(acac)_3$ (2 mmol), 1,2-hexadecanediol (10 mmol), oleic acid (6 mmol), oleylamine (6 mmol), and benzyl ether (20 mL) were charged in a 100 mL three-neck round-bottom flask and magnetically stirred under a flow of nitrogen. The mixture was first heated to 110 °C for 1 h to remove moisture. Then, the temperature was increased to 210 °C for 1 h and was finally refluxed for 1 h before cooling down to room temperature. The black−brown mixture was precipitated, washed three times using ethanol, and then dispersed in hexane. The composition was changed by choosing different precursors and their ratios. $Fe_3O_4/Zn_{0.2}Mn_{0.8}Fe_2O_4$ nanoparticles were synthesized by adding $Mn(acac)_2$ (2 mmol) and $Zn(acac)_2$ (1 mmol) under identical conditions.

Functionalization of Single Phase and Core/Shell Magnetic Nanostructures. To convert from hydrophobic to hydrophilic nature, the as-synthesized oleic acid coated hydrophobic core/shell (or single phase) magnetic nanostructures were functionalized with the citrate via the ligand exchange process. The as-synthesized oleic acid coated hydrophobic nanostructures were functionalized with citrate via the ligand exchange process, resulting in hydrophilic MNS.[30,32] The particle diameters and size distribution were determined from transmission electron microscopy (TEM). The final concentration of the Fe, Mn, and Zn in MNS was determined by inductively coupled plasma mass spectrometry (ICP-MS) analysis.

Structural and Magnetic Characterization. The seed mediated growth is confirmed by TEM and energy dispersive X-ray (EDX) using Hitachi H8100 TEM (200 kV) and Hitachi HD2300 (200 kV), respectively. M−H hysteresis loops and field-cooled (FC)/zero-field-cooled (ZFC) magnetization curves were recorded using a physical property measurement system (Quantum Design Dyanacool-PPMS).
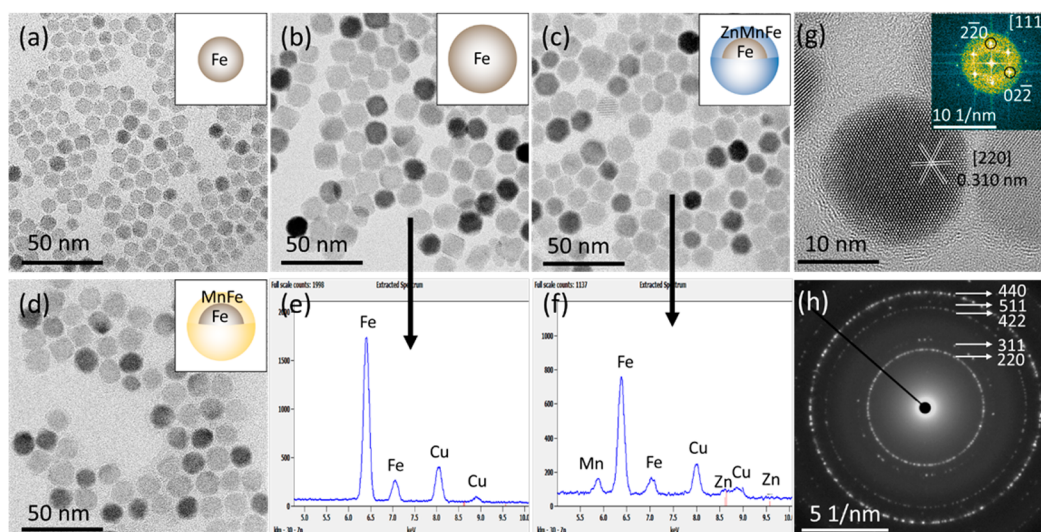
Figure 2. TEM images of (a) 8 nm Fe_3O_4 nanoparticles, (b) 12 nm Fe_3O_4, (c) 12 nm $Fe_3O_4@Zn_{0.2}Mn_{0.8}Fe_2O_4$, and (d) 12 nm $Fe_3O_4/MnFe_2O_4$ core/shell nanostructures. EDX of (e) 12 nm Fe_3O_4 and (f) 12 nm $Fe_3O_4/ Zn_{0.2}Mn_{0.8}Fe_2O_4$ core/shell nanostructures. (g) HRTEM and (h) SAED of $Fe_3O_4/MnFe_2O_4$ MNS.

The stoichiometry of core/shell and single phase MNS is confirmed via ICP-MS. To calculate saturation magnetization (emu/g), the masses of all metals (Fe and/or Zn and/or Mn) were considered which was calculated via ICP-MS. An additional TEM image, SAED pattern, and EDX profiles were acquired using JEOL Grand ARM 300F TEM. A HAADF STEM image and corresponding EELS profiles were obtained using a JEOL ARM 200F TEM.

Measurement of r_2 Relaxivity. MFe_2O_4 magnetic nanostructures dispersed in water were diluted to concentrations ranging from 0.01 to 0.11 mM of metal ion. T_2 relaxation times were determined at 3.0 T Magnetom Verio (Siemens Healthcare, Erlangen, Germany) using the multiple-echo-fast-spin-echo sequence. The multiple-echo-spin-echo sequence has the following parameters: TR = 1290 ms, 8 echo times starting with 9.9 to 79.2 ms, 160 mm FOV, 256 × 256 matrix, and slice thickness of 3 mm. Given that we had multiple samples with a distribution of T_2 relaxation times, we had to limit the range of echo times; the echo time range may not be optimal for every sample. A commercial 12 channel head coil (diameter ~160 mm) was used. A 1.5 mL eppendorf centrifuge tube was used as a sample holder. R_2 maps were generated using a custom software using Matlab. The signal decay was fit to a single exponential function to estimate T_2 on a pixel by pixel basis. To calculate r_2 relaxivity, masses of all metals (Fe and/or Zn and/or Mn) were considered which was calculated via ICP-MS.

Thermal Activation. Thermal activation experiments were performed on an MSI Automation Inc. Hyperthermia Research System RF generator at a frequency of 300 kHz and a power of 5 kW. A 0.2 mL suspension was placed inside the 5 cm coil generating the AC magnetic field of 5 kA/m. A nonmagnetic nonmetallic optical temperature probe (Fiso) was used to monitor the temperature. Each experiment time duration was 15 min. SAR was calculated from the thermal activation plots using the following equation

$$SAR = \frac{CV_s}{m}\left(\frac{dT}{dt}\right) \tag{1}$$

where C is the specific heat capacity of the solvent, dT/dt is the initial slope of the thermal activation plot, V_s is the sample volume, and m is mass of magnetic material in the sample.

■ RESULTS AND DISCUSSION

To synthesize core/shell MNS, we have selected Fe_3O_4, $MnFe_2O_4$, and $Zn_{0.2}Mn_{0.8}Fe_2O_4$ for this study since they have shown different anisotropic behaviors in our previous studies.[30]

If used as a core and shell combination, their different anisotropy can result in exchange interactions at the core/shell interface.[30] We have used the seed mediated approach for synthesis where MFe_2O_4 nanoparticles are used as seeds (labeled as core MNS) to grow shell of the same or different material. For example, when Fe_3O_4 core MNS are used as seeds, addition of Mn and Mn+Zn precursor results in $Fe_3O_4/MnFe_2O_4$ and $Fe_3O_4/Zn_{0.2}Mn_{0.8}Fe_2O_4$ (labeled as core/shell MNS), respectively, while addition of Fe precursor results in larger size Fe_3O_4 (labeled as single phase MNS) that have been used as a control. Similarly, $MnFe_2O_4$ and $Zn_{0.2}Mn_{0.8}Fe_2O_4$ core MNS are used as seeds to prepare a library of core/shell and single phase MNS (Figure 1). For magnetic characterization (magnetization loops, anisotropy, and susceptibility) and theranostic characterization (contrast enhancement and thermal activation), the samples are divided into four sets. In set 1 samples, the core is kept constant as Fe_3O_4 while the shell is varied from Fe_3O_4 to $MnFe_2O_4$ and $Zn_{0.2}Mn_{0.8}Fe_2O_4$. In set 2, Fe_3O_4 shell is kept constant and core is varied from Fe_3O_4 to $MnFe_2O_4$ and $Zn_{0.2}Mn_{0.8}Fe_2O_4$. In set 3, single phase Fe_3O_4 and $MnFe_2O_4$ MNS are compared with their core/shell counterparts $Fe_3O_4/MnFe_2O_4$ or $MnFe_2O_4/Fe_3O_4$. In set 4, single phase $MnFe_2O_4$ and $Zn_{0.2}Mn_{0.8}Fe_2O_4$ MNS are compared with their core/shell counterparts $MnFe_2O_4/Zn_{0.2}Mn_{0.8}Fe_2O_4$ or $Zn_{0.2}Mn_{0.8}Fe_2O_4/MnFe_2O_4$. The size of all core/shell and single phase MNS is kept constant to avoid any size effect on magnetic and theranostic properties.

The seed mediated growth is confirmed by transmission electron microscopy (TEM) and energy dispersive X-ray (EDX). The size of core MNS is kept as 8 nm, while size of the core/shell and the single phase MNS is kept as 12 nm. Figure 2a−d shows TEM images of 8 nm Fe_3O_4 core MNS, 12 nm Fe_3O_4 single phase MNS, 12 nm $Fe_3O_4/MnFe_2O_4$, and 12 nm $Fe_3O_4/Zn_{0.2}Mn_{0.8}Fe_2O_4$ core/shell MNS. The shell thickness is tuned by controlling the amount of core MNS during synthesis of core/shell MNS while the amount of shell precursors is kept constant. The TEM images of core/shell MNS do not show distinguished core and shell structure since the lattice mismatch and contrast between Fe_3O_4, $MnFe_2O_4$, and $Zn_{0.2}Mn_{0.8}Fe_2O_4$ is negligible, as reported previously.[14,15,22]

In energy dispersive X-ray (EDX), Fe_3O_4 single phase MNS shows only Fe peaks and $Fe_3O_4/Zn_{0.2}Mn_{0.8}Fe_2O_4$ core/shell MNS shows the presence of Mn and Zn peaks in addition to the Fe peak, confirming the $Zn_{0.2}Mn_{0.8}Fe_2O_4$ shell coating on Fe_3O_4 nanoparticles (Figure 2e,f). Figure 2g,h shows a high resolution TEM (HRTEM) image and selected area electron diffraction (SAED) pattern of $Fe_3O_4/MnFe_2O_4$ MNS, confirming the crystalline nature of the particle and spinel AB_2O_4 crystal structure.

However, to show the direct evidence of core/shell structure, MNS are characterized via electron energy loss spectroscopy (EELS). Elemental analysis is done on a single $Fe_3O_4/MnFe_2O_4$ MNS via core loss and a low loss line scan and area map (Figures 3 and S1). Figure 3 shows elemental
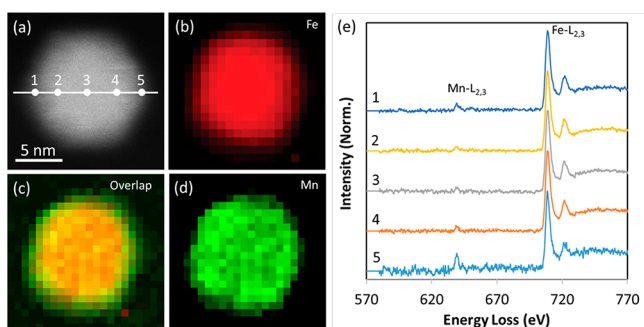

Figure 3. (a) High angle annular dark field scanning transmission electron microscopy (HAADF-STEM) image and (b−d) elemental EELS (core loss) maps of $Fe_3O_4/MnFe_2O_4$ MNS. While the Fe map is dominant in the core region, the Mn map is dominant in the shell region, and the overlap image clearly shows the difference in intensity of Mn at the core and shell region. (e) Elemental EELS (core loss) line scan and corresponding $Fe-L_{2,3}$ and $Mn-L_{2,3}$ intensity peaks of $Fe_3O_4/MnFe_2O_4$ MNS. The normalized profiles were used to confirm the relative intensity of Mn compared to the Fe edge. At different points (1−5), from edge to center to edge, intensity of Mn is compared as shown in (a). At the edges, the intensity of Mn is noticeable, but as we move toward the center, the Mn intensity drops significantly due to the dominant signal from the Fe_3O_4 core. The higher Mn signal at the edges compared to the center confirms uniform $MnFe_2O_4$ shell on Fe_3O_4 nanostructures.

EELS (core loss) line scan and area maps. An elemental EELS line scan was done at five different points from edge to center to edge (Figure 3a), and corresponding Fe and Mn intensity peaks are shown in Figure 3e. The Fe peak has been normalized, and the intensity of Mn is compared. At edges, the intensity of Mn is noticeable, but as we move toward the center, the Mn intensity drops significantly due to the dominant signal from the Fe_3O_4 core. Figure 3a−d elemental EELS maps of $Fe_3O_4/MnFe_2O_4$ MNS. In the Fe map (Figure 3b), the presence of Fe can be seen throughout the particle, and as expected, the intensity is higher in the core region than the edge. However, in the Mn map (Figure 3d), Mn is more dominant in the edges than the center and it is clearer in the overlap image (Figure 3c). The higher Mn signal at the edges compared to the center in both line scan and area maps confirm uniform $MnFe_2O_4$ shell on Fe_3O_4 nanostructures.

Figure 4 shows magnetization−field (M−H) loops of 12 nm single phase and core/shell MNS (sets 1 and 2) measured at room temperature (RT) and 10 K. At RT, all the core/shell and single phase MNS show no hysteresis and demonstrate superparamagnetic behavior which is ideal for their use in

biomedical applications (Figure 4a,b). For the set 1 samples, saturation magnetization for 12 nm $Fe_3O_4/Zn_{0.2}Mn_{0.8}Fe_2O_4$ and 12 nm $Fe_3O_4/MnFe_2O_4$ core/shell MNS is found to be 95 and 86 emu/g, respectively, higher than 12 nm Fe_3O_4 MNS (76 emu/g). Similarly, for the set 2, saturation magnetization of $Zn_{0.2}Mn_{0.8}Fe_2O_4/Fe_3O_4$ (91 emu/g) and $MnFe_2O_4/Fe_3O_4$ (82 emu/g) core/shell MNS is found to be higher than 12 nm single phase Fe_3O_4 MNS. In both cases, core/shell MNS with $Zn_{0.2}Mn_{0.8}Fe_2O_4$ show the highest saturation magnetization followed by core/shell MNS with $MnFe_2O_4$. Single phase Fe_3O_4 MNS show the lowest saturation magnetization in sets 1 and 2. It is expected to observe this trend since saturation magnetization of $MnFe_2O_4$ and $Zn_{0.2}Mn_{0.8}Fe_2O_4$ has been observed to be higher than that of Fe_3O_4.[30] Hence, their presence could have substantial impact on the saturation magnetization of the core/shell MNS.

However, when M−H loops of core/shell and single phase MNS are measured at 10 K, we made two key observations (Figure 4c,d). First, the M−H loops measured at 10 K show hysteresis, indicating their ferromagnetic behavior. As expected, the saturation magnetization of all the samples (core/shell and single phase MNS) at 10 K is observed to be higher than the saturation magnetization measured at RT.[33] Second and more important, no kink is observed in the hysteresis loops of all core/shell MNS measured at 10 K. Previously, it has been reported that, when two different ferrite nanoparticles are physically mixed together, it results in kink in their hysteresis loops due to lack in exchange interactions between them, resulting in two phase behavior. Although each spinel ferrite shows different magnetic behavior (saturation magnetization, remanent magnetization, and coercivity) at 10 K (Figure S2), the B−H hysteresis loops of core/shell MNS at RT show smooth permeability or change in magnetic flux density with field, suggesting intimate contact and exchange coupling between core and shell ferrite (Figure S3). These results show a typical exchange spring behavior, similar to what has been reported for the hard/soft mutlilayer composites.[34−36]

Since it is hard to see any direct effect of exchange coupling on saturation magnetization, we have recorded susceptibility plots by measuring magnetization of core/shell and single phase MNS samples at magnetic fields from 0 to 4 T at RT. To determine susceptibility independent of saturation magnetization, we have normalized the susceptibility plots. For sets 1 and 2, the core (or shell) is replaced from Fe_3O_4 to $MnFe_2O_4$ and $Zn_{0.2}Mn_{0.8}Fe_2O_4$; an increase in magnetic susceptibility is observed (Figure 5a,b). In addition to sets 1 and 2, susceptibility of Fe_3O_4 and $MnFe_2O_4$ single phase MNS has been compared with their core/shell counterparts $Fe_3O_4/$ $MnFe_2O_4$ and $MnFe_2O_4/Fe_3O_4$ (set 4 samples). Similarly, $MnFe_2O_4$ and $Zn_{0.2}Mn_{0.8}Fe_2O_4$ single phase MNS are compared with $MnFe_2O_4/Zn_{0.2}Mn_{0.8}Fe_2O_4$ and $Zn_{0.2}Mn_{0.8}Fe_2O_4/MnFe_2O_4$ (set 4 samples). In both sets 3 and 4, susceptibility of the single phase MNS is observed to be lower than their core/shell counterparts.

Since the M−H loops of both core/shell and single phase MNS show a superparamagnetic and ferromagnetic nature at RT and 10 K, respectively, their blocking temperature is expected to be between these two temperatures. To find out the blocking temperature, zero-field-cooling (ZFC) magnetization plots of core/shell and single phase MNS are measured at 100 Oe (Figure 6). Here, the key result to observe is that all core/shell MNS show a single peak in ZFC plots, confirming exchange coupling between core and shell ferrites.[15,22]
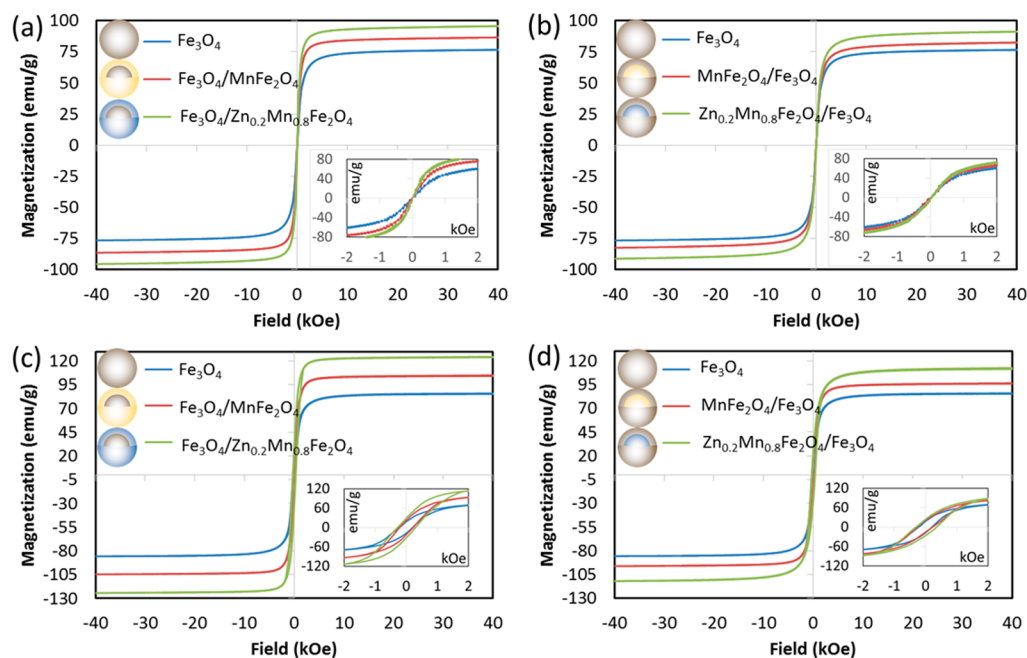
Figure 4. Magnetization−field (M−H) loops of set 1 (Fe_3O_4, $Fe_3O_4/MnFe_2O_4$, $Fe_3O_4/Zn_{0.2}Mn_{0.8}Fe_2O_4$) and set 2 ($Fe_3O_4$, $MnFe_2O_4/Fe_3O_4$, $Zn_{0.2}Mn_{0.8}Fe_2O_4/Fe_3O_4$) samples at RT and 10 K. (a, b) At RT, both set samples show superparamagnetic behavior. (c, d) At 10 K, hysteresis is observed in both sets of samples, demonstrating the ferromagnetic nature.
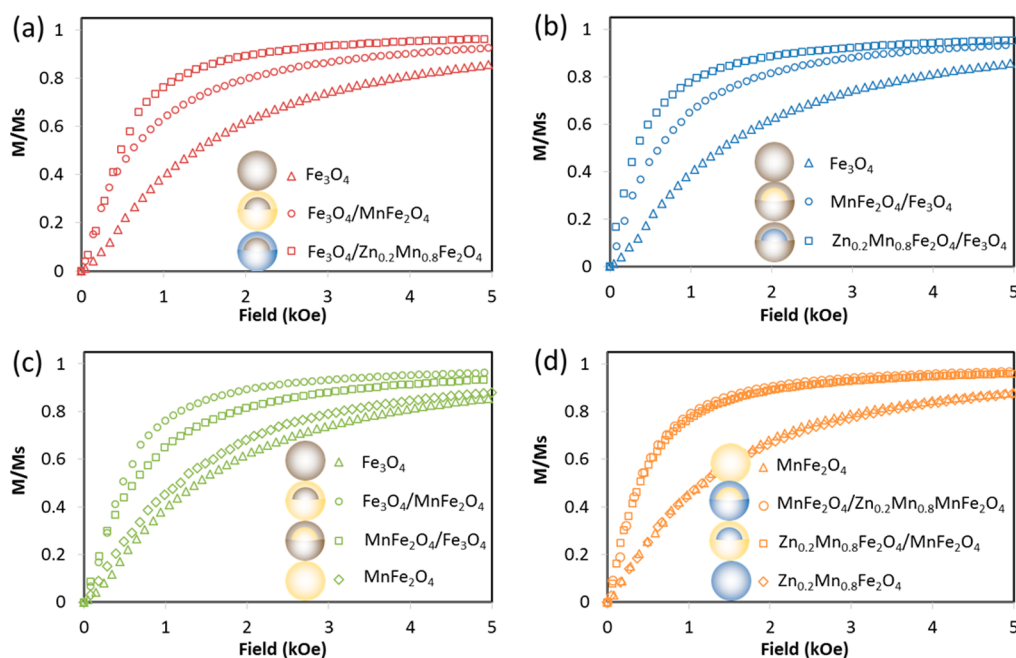

Figure 5. Normalized magnetic susceptibility plots of set 1 (Fe_3O_4, $Fe_3O_4/MnFe_2O_4$, $Fe_3O_4/Zn_{0.2}Mn_{0.8}Fe_2O_4$), set 2 ($Fe_3O_4$, $MnFe_2O_4/Fe_3O_4$, $Zn_{0.2}Mn_{0.8}Fe_2O_4/Fe_3O_4$), set 3 ($Fe_3O_4$, $MnFe_2O_4$, $Fe_3O_4/MnFe_2O_4$, $MnFe_2O_4/Fe_3O_4$), and set 4 ($MnFe_2O_4$, $Zn_{0.2}Mn_{0.8}Fe_2O_4$, $MnFe_2O_4/Zn_{0.2}Mn_{0.8}Fe_2O_4$, $Zn_{0.2}Mn_{0.8}Fe_2O_4/MnFe_2O_4$) samples. (a, b) In sets 1 and 2, the shell (or core) is changed from Fe_3O_4 to $MnFe_2O_4$ and $Zn_{0.2}Mn_{0.8}Fe_2O_4$; magnetic susceptibility increases. (c, d) In sets 3 and 4, core/shell MNS show higher magnetic susceptibility than their single phase counterparts.

Blocking temperature of core/shell MNS is found to be significantly higher than that of single phase MNS. For set 1 samples, when the shell is changed from Fe_3O_4 to $MnFe_2O_4$ and $Zn_{0.2}Mn_{0.8}Fe_2O_4$, blocking temperature is increased from 90 K to 162 K and 265 K, respectively (Figure 6a). Similarly, for set 2 samples, when the core is changed from Fe_3O_4 to $MnFe_2O_4$ and $Zn_{0.2}Mn_{0.8}Fe_2O_4$, blocking temperature is increased from 90 K to 157 K and 222 K, respectively (Figure

5b). It is well-known that blocking temperature is strongly dependent on the size of the MNS.[37−40] However, in this case since the size of single phase and core/shell MNS is similar, the higher blocking temperature could be correlated to the higher effective anisotropy of core/shell MNS.[15,41,42] Other than shift, broadening of the ZFC peak is also observed in the core/shell MNS samples. Often, the broadening has been correlated with the large size distribution of MNS.[43] However, since the size
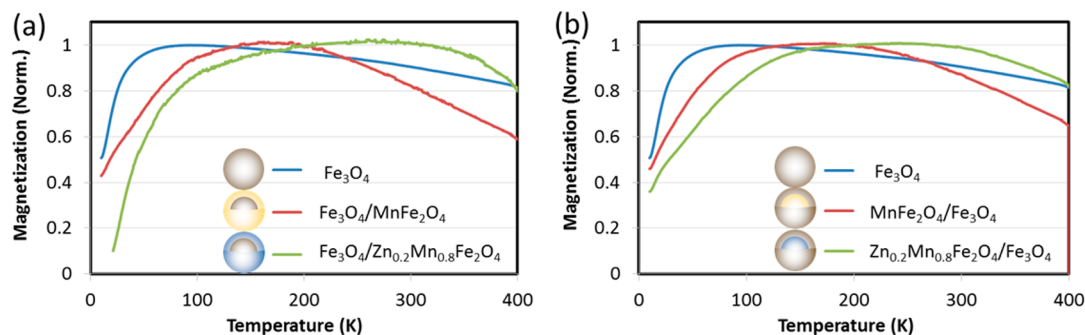
Figure 6. Zero-field cooling (ZFC) curves of (a) set 1 (Fe_3O_4, $Fe_3O_4/MnFe_2O_4$, $Fe_3O_4/Zn_{0.2}Mn_{0.8}Fe_2O_4$) and (b) set 2 ($Fe_3O_4$, $MnFe_2O_4/Fe_3O_4$, $Zn_{0.2}Mn_{0.8}Fe_2O_4/Fe_3O_4$) samples. When the shell (or core) is changed from Fe_3O_4 to $MnFe_2O_4$ and $Zn_{0.2}Mn_{0.8}Fe_2O_4$, blocking temperature is increased in both sets.

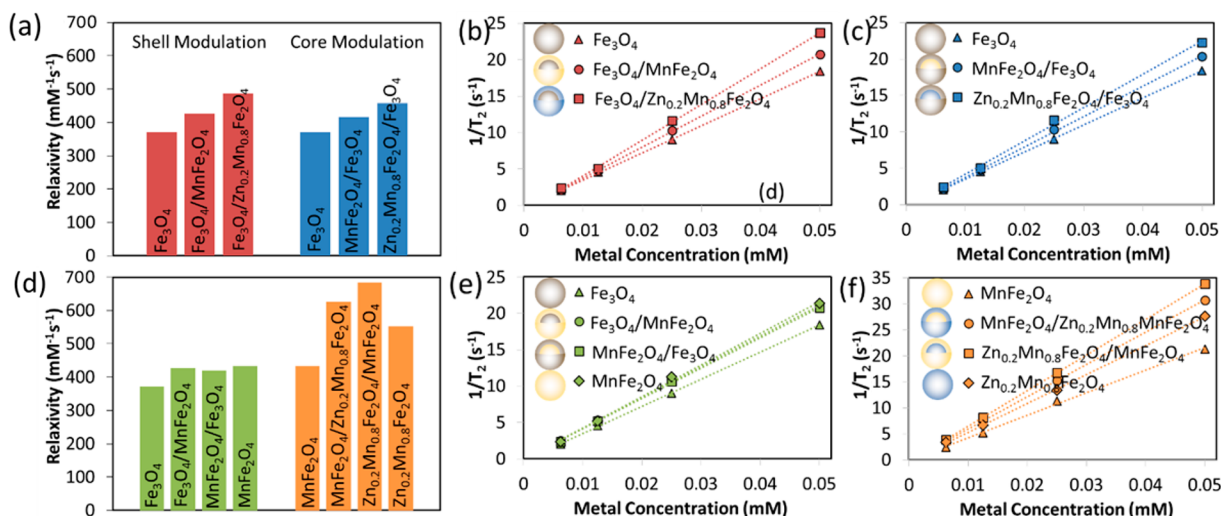**Figure 7.** Comparison of r_2 relaxivity (a, d) values and (b, c, e, f) plots of set 1 (Fe_3O_4, $Fe_3O_4/MnFe_2O_4$, $Fe_3O_4/Zn_{0.2}Mn_{0.8}Fe_2O_4$), set 2 ($Fe_3O_4$, $MnFe_2O_4/Fe_3O_4$, $Zn_{0.2}Mn_{0.8}Fe_2O_4/Fe_3O_4$), set 3 ($Fe_3O_4$, $MnFe_2O_4$, $Fe_3O_4/MnFe_2O_4$, $MnFe_2O_4/Fe_3O_4$), and set 4 ($MnFe_2O_4$, $Zn_{0.2}Mn_{0.8}Fe_2O_4$, $MnFe_2O_4/Zn_{0.2}Mn_{0.8}Fe_2O_4$, $Zn_{0.2}Mn_{0.8}Fe_2O_4/MnFe_2O_4$) samples. (a–c) In sets 1 and 2, the shell (or core) is changed from Fe_3O_4 to $MnFe_2O_4$ and $Zn_{0.2}Mn_{0.8}Fe_2O_4$, and r_2 relaxivity increases. (c, d) In sets 3 and 4, core/shell MNS show higher r_2 relaxivity than their single phase counterparts.

distribution of the core/shell MNS is very narrow in our case, the broadening can be explained due to the increased interparticle interactions that arise from either dipolar interactions between MNS or the exchange interactions between the magnetic ions at the surface of the nanoparticles.[44]

Magnetic nanostructures have been used successfully as T_2 contrast agents in magnetic resonance imaging (MRI). The T_2 contrast enhancement effect of MNS is measured by r_2 relaxivity, a slope of relaxation rate R_2 (s^{-1}) plotted against MNS metal concentration (mM). The higher relaxivity corresponds to higher T_2 contrast enhancement effect. The R_2 relaxation rate of MNS is defined as

$$R_2 = \frac{1}{T_2} = \frac{256\pi^2\gamma^2}{405} M_s^2 V \frac{r^2}{D\left(1 + \frac{L}{r}\right)} \tag{2}$$

where T_2 is transverse relaxation time, γ is proton gyromagnetic ratio, M_s is saturation magnetization, V is volume of MNS, D is diffusion coefficient of water molecules, r is radius of MNS core, and L is thickness of MNS surface coating.[45] On the basis of eq 2 and previously reported results, r_2 is shown to be dependent on saturation magnetization and

susceptibility of MNS.[30,46,47] In Figure 7, r_2 relaxivity values and plots of 12 nm core/shell MNS have been compared with same size single phase MNS. The spin–spin relaxation time (T_2) is observed at 3 T. Consistent with the magnetization and susceptibility data, core/shell MNS show higher r_2 relaxivity than similar size single phase MNS. For the set 1 samples, when the shell is changed from Fe_3O_4 to $MnFe_2O_4$ and $Zn_{0.2}Mn_{0.8}Fe_2O_4$, relaxivity increases from 372 $mM^{-1}s^{-1}$ to 427 $mM^{-1}s^{-1}$ and 487 $mM^{-1}s^{-1}$, respectively (Figure 7a). Similarly, for set 2 samples, when the core is changed from Fe_3O_4 to $MnFe_2O_4$ and $Zn_{0.2}Mn_{0.8}Fe_2O_4$, SAR increases from 372 $mM^{-1}s^{-1}$ to 416 $mM^{-1}s^{-1}$ and 457 $mM^{-1}s^{-1}$, respectively (Figure 7b). In both sets, the increase in relaxivity suggests that exchange coupling between Fe_3O_4 and $MnFe_2O_4$ (or $Zn_{0.2}Mn_{0.8}Fe_2O_4$) has an impact on relaxivity. However, it should also be noted that core $MnFe_2O_4$ and $Zn_{0.2}Mn_{0.8}Fe_2O_4$ show higher relaxivity than Fe_3O_4, as reported previously.[30,46,47] So, one of the reasons for this increasing trend could be higher relaxivity of $MnFe_2O_4$ and $Zn_{0.2}Mn_{0.8}Fe_2O_4$. Hence, to observe the direct effect of exchange coupling, r_2 relaxivity of Fe_3O_4 and $MnFe_2O_4$ MNS has been compared with their core/shell counterparts $Fe_3O_4/MnFe_2O_4$ and $MnFe_2O_4/Fe_3O_4$ (set 3 samples). Similarly, $MnFe_2O_4$ and
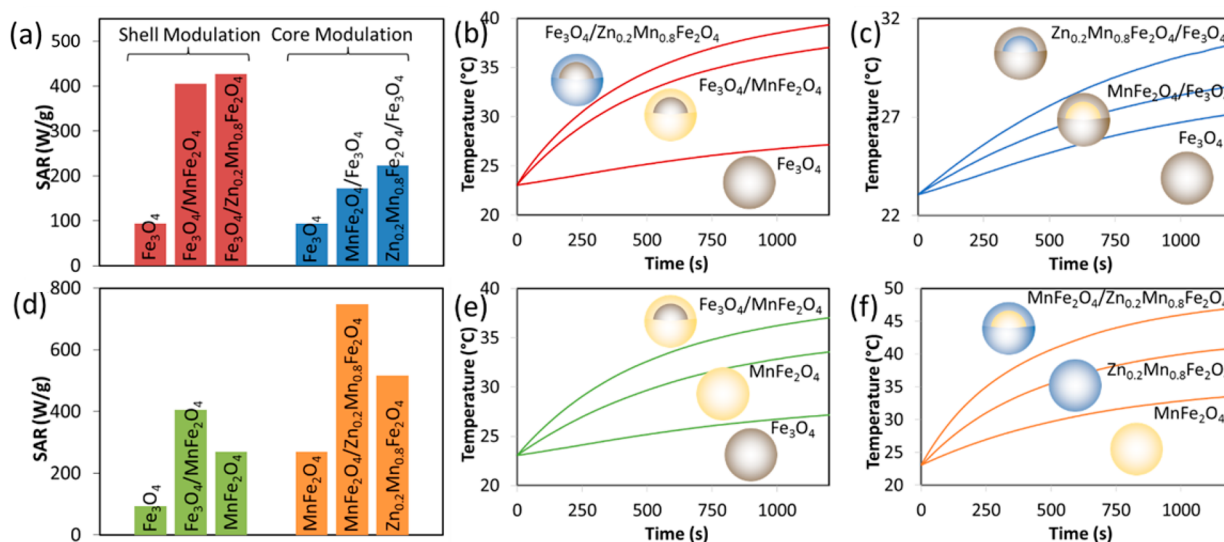
Figure 8. Comparison of (a, d) SAR values and (b, c, e, f) RF field induced thermal activation plots of set 1 (Fe_3O_4, $Fe_3O_4/MnFe_2O_4$, $Fe_3O_4/Zn_{0.2}Mn_{0.8}Fe_2O_4$), set 2 ($Fe_3O_4$, $MnFe_2O_4/Fe_3O_4$, $Zn_{0.2}Mn_{0.8}Fe_2O_4/Fe_3O_4$), set 3 ($Fe_3O_4$, $MnFe_2O_4$, $Fe_3O_4/MnFe_2O_4$), and set 4 ($MnFe_2O_4$, $Zn_{0.2}Mn_{0.8}Fe_2O_4$, $MnFe_2O_4/Zn_{0.2}Mn_{0.8}Fe_2O_4$) samples. (a) In sets 1 and 2, the shell (or core) is changed from Fe_3O_4 to $MnFe_2O_4$ and $Zn_{0.2}Mn_{0.8}Fe_2O_4$; RF induced temperature as well as SAR increase. (d) In sets 3 and 4, core/shell MNS show higher RF induced temperature and SAR than their single phase counterparts. The size of all MNS (single phase or core/shell) is 12 nm.

$Zn_{0.2}Mn_{0.8}Fe_2O_4$ MNS are compared with $MnFe_2O_4/Zn_{0.2}Mn_{0.8}Fe_2O_4$ and $Zn_{0.2}Mn_{0.8}Fe_2O_4/MnFe_2O_4$ (set 4 samples). For set 3 and 4 samples, high r_2 relaxivity of core/shell MNS compared to single phase MNS confirms that exchange coupling between two ferrites can result in significantly higher relaxivity in core/shell MNS (Figure 7c,d). After optimizing the core and shell combination, the highest r_2 relaxivity of up to 684 $mM^{-1}s^{-1}$ is obtained, that is ~7 times higher than Ferumoxtran (dextran coated iron oxide nanoparticles), an FDA approved T_2 contrast agent for MRI.[48] It means, when used as a contrast agent, core/shell MNS can generate 7 times higher signal than Ferumoxtran, or if the signal is already sufficient, administration dosages can be decreased by 7 times.

MNS can be thermally activated and generate heat under an external RF field that makes the MNS unique for noninvasive therapeutic applications in biomedicine.[49] Rosensweig[50] described the analytical relationships and computational models of thermal activation in a suspension of MNS under an external RF field. Thermal activation of the MNS under an external RF field is quantified as specific absorption rate (SAR), that is the amount of heat generated per unit gram of the MNS. Higher SAR is critical in order to obtain high therapeutic efficacy of MNS in biomedical applications. The SAR for monodisperse magnetic nanostructures under an external RF field can be calculated as

$$SAR \propto m_s^2 \mathbf{H}_0^2 f V \frac{2\pi f \tau}{1 + (2\pi f \tau)^2} \qquad (3)$$

where $\mathbf{H}_0$ is the magnetic field intensity, f is frequency, m_s is saturation magnetization of MNS, V is MNS volume, and τ is effective relaxation time and depends on Brownian (τ_B) and Néel (τ_N) relaxation time as given by

$$\frac{1}{\tau} = \frac{1}{\tau_B} + \frac{1}{\tau_N} \qquad (4)$$

The dominant mechanism is the one which has shortest relaxation time. If $\tau_B \ll \tau_N$ then $\tau = \tau_B$ while if $\tau_B \gg \tau_N$ then $\tau = \tau_N$. It has been reported that in superparamagnetic nanoparticles of size smaller than 16 nm, $\tau_B \gg \tau_N$ so heating mainly arises due to Néel relaxation which can be calculated as[51]

$$\tau_N = \tau_0 \exp\left(\frac{K_u V_m}{k_B T}\right) \qquad (5)$$

where τ_0 is constant, K_u is the anisotropic constant of MNS, V_m is volume of MNS, k_B is Boltzmann's constant, and T is temperature. According to eqs 3 and 5, the SAR depends on many factors. For our experiments, factors such as $\mathbf{H}_0$, f, and V are constant, and magnetization and anisotropy are the contributing factors for SAR. Figure 8 shows the thermal activation plots and SAR values of core/shell and single phase MNS under RF field of 5 kA/m (5 kW, 300 kHz). The field ($\mathbf{H}_0$) and frequency (f) is chosen such that the $\mathbf{H}_0 f$ factor is well below the experimentally estimated threshold of 5×10^9 A/ms.[52] The concentration of both core/shell and single phase MNS is kept the same to avoid any concentration dependence effect on SAR. Consistent with anisotropy and magnetization data (Figures 4 and 6), the calculated SAR values based on the thermal activation plots show that core/shell MNS show superior thermal activation properties over single phase MNS (Figure 8a). For the set 1 samples, when the shell is changed from Fe_3O_4 to $MnFe_2O_4$ and $Zn_{0.2}Mn_{0.8}Fe_2O_4$, SAR increases from 93 W/g to 405 W/g and 427 W/g, respectively. Similarly, for set 2 samples, when the core is changed from Fe_3O_4 to $MnFe_2O_4$ and $Zn_{0.2}Mn_{0.8}Fe_2O_4$, SAR increases from 93 W/g to 172 W/g and 223 W/g, respectively. In the past, we have shown that core $MnFe_2O_4$ and $Zn_{0.2}Mn_{0.8}Fe_2O_4$ show higher anisotropy than Fe_3O_4.[30] As we replace the core (or shell) component from Fe_3O_4 to $MnFe_2O_4$ and $Zn_{0.2}Mn_{0.8}Fe_2O_4$, the exchange coupling due to the difference in anisotropy between core and shell causes higher thermal activation and hence higher SAR.[10,14]
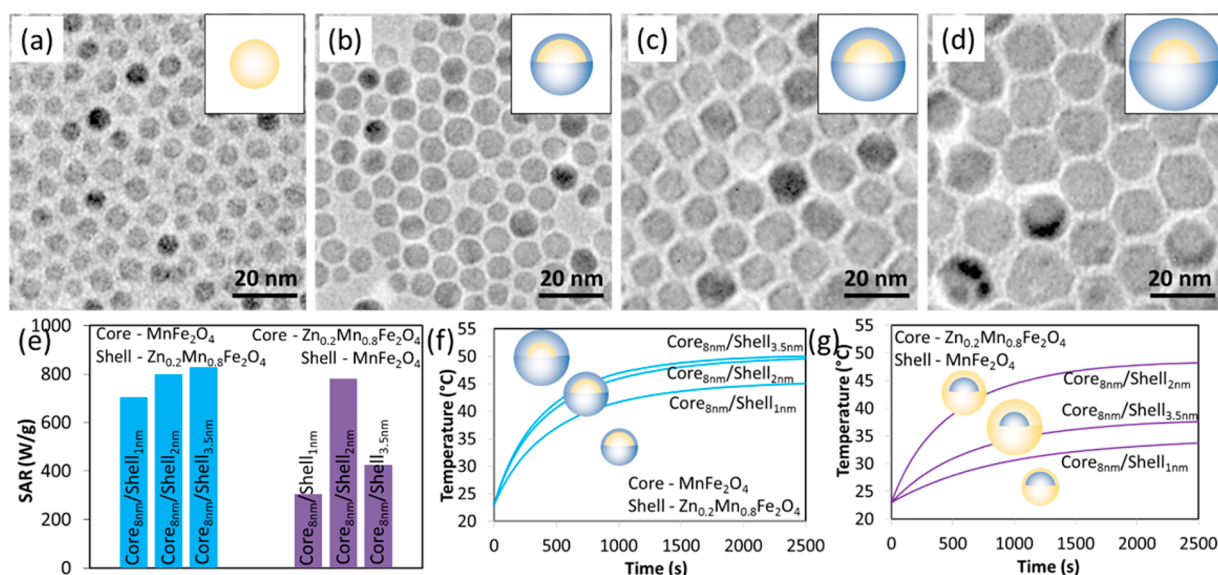
Figure 9. Optimization of thermal activation properties of core/shell MNS where core size is kept constant as 8 nm while the shell is tuned from 1 to 3.5 nm. TEM images of (a) 8 nm $MnFe_2O_4$ and (b) 10 nm, (c) 12 nm, and (d) 15 nm $MnFe_2O_4/Zn_{0.2}Mn_{0.8}Fe_2O_4$ core/shell MNS. SAR and thermal activation plots of (e, f) $MnFe_2O_4/Zn_{0.2}Mn_{0.8}Fe_2O_4$ and (e, g) $Zn_{0.2}Mn_{0.8}Fe_2O_4/MnFe_2O_4$ core/shell MNS show that exchange coupling is critically dependent on proportion and dimension of core and shell component in core/shell MNS.

Similar to r_2 relaxivity, SAR of 12 nm $Fe_3O_4/MnFe_2O_4$ MNS is compared with that of 12 nm Fe_3O_4 and 12 nm $MnFe_2O_4$ (set 3 samples). The SAR value of 12 nm $Fe_3O_4/MnFe_2O_4$ core/shell MNS is found to be 405 W/g, 1.5 times higher than 12 nm $MnFe_2O_4$ (269 W/g) and around 4.5 times higher than 12 nm Fe_3O_4 nanostructures (93 W/g) (Figure 8b). A similar trend is observed for $MnFe_2O_4/Zn_{0.2}Mn_{0.8}Fe_2O_4$ core/shell MNS over 12 nm $MnFe_2O_4$ and 12 nm $Zn_{0.2}Mn_{0.8}Fe_2O_4$ nanoparticles (set 4 samples). After optimizing the core and shell combination, the highest SAR of up to 748 W/g is obtained. This change in SAR suggests that, for core/shell MNS, exchange coupling can enhance anisotropy which directly affects their thermal activation properties. The relationship between anisotropy and SAR has been well established theoretically and experimentally.[53−59] Carrey et al. have shown the calculation of SAR as a function of the MNP anisotropy and have shown that an optimum anisotropy increases the SAR.[53,54] Overall, we have shown that, by just changing the morphology from single phase to core/shell and controlling their composition, the RF field induced heating temperatures can be increased from 26 °C to the temperature range that is considered ideal for targeted therapy (43−47 °C). For diseases such as cancer, MNS under application of the RF field can specifically kill cancer cells at these temperatures without affecting any normal cells, thus making the treatment noninvasive and without any side effect.[19]

The key parameters to obtain effective exchange coupling are the size and proportion of hard (higher anisotropy) and soft (lower anisotropy) magnetic components.[1,2,5] For core/shell MNS, optimization of exchange coupling has been achieved by tuning the core diameter and shell thickness.[4] Since FePt nanoparticles are highly anisotropic,[60] the soft magnetic Fe_3O_4 shell was coated with a thickness of 0.5 to 3 nm, resulting in exchange-coupled $FePt/Fe_3O_4$ core/shell MNS. The highest energy product was achieved with an optimum 1 nm Fe_3O_4 shell thickness.[4] For shell thickness of 0.5 nm, the soft magnetic component was not sufficient, while for shell thickness higher than 1 nm, the soft magnetic

component was too high, resulting in lower energy products. On the basis of this motivation, we have optimized the thermal activation properties of core/shell MNS by tuning dimension and ratio of core and shell components. Core/shell MNS with 8 nm core with 1, 2, and 3.5 nm shell thickness are prepared, resulting in particle diameter of 10, 12, and 15 nm (Figure 9a−d). $MnFe_2O_4$ and $Zn_{0.2}Mn_{0.8}Fe_2O_4$ as core and shell (or vice versa) are selected for the study due to their higher theranostic properties among all core/shell combinations. For both sets, the thermal activation properties of the core/shell MNS changed significantly when the shell thickness is tuned from 1 to 3.5 nm (Figure 9e−g). When $Zn_{0.2}Mn_{0.8}Fe_2O_4$ core is kept constant, RF heating temperature increases first when the $MnFe_2O_4$ shell thickness is increased from 1 to 2 nm. When the shell thickness is further increased to 3.5 nm, the RF heating temperature reduces (Figure 9f). Since anisotropy of $MnFe_2O_4$ is lower than $Zn_{0.2}Mn_{0.8}Fe_2O_4$, exceedingly higher amounts (3.5 nm shell) of $MnFe_2O_4$ can result in overall lower anisotropy of core/shell MNS, resulting in a decrease in RF heating temperature. When $MnFe_2O_4$ core is kept constant and $Zn_{0.2}Mn_{0.8}Fe_2O_4$ shell thickness is tuned, RF heating temperature increases first when the shell thickness is increased from 1 to 2 nm and then stays almost the same when the shell thickness is further increased to 3.5 nm (Figure 9g). By just interchanging core and shell materials, we observe a different trend since the proportion of high and low anisotropic phases changes, indicating exchange coupling is also significantly dependent on the proportion of each ferrite. After the optimization process, the highest SAR of up to 827 W/g is obtained, that is ∼9 times higher than single phase Fe_3O_4 MNS. These results indicate that an optimum dimension and proportion of core and shell components are required to obtain maximum exchange coupling. A similar trend was demonstrated by Machado and co-workers.[61] They tested $CoFe_2O_4−CoFe_2$ core−shell nanoparticles with shell thickness ranging from 1.2 to 11.0 nm. The thickness for optimum exchange coupling was found to be 7.8 nm.

CONCLUSIONS

We have demonstrated exchange coupling in core/shell magnetic nanostructures (MNS) where both core and shell components are composed of soft magnetic ferrites (Fe_3O_4, $MnFe_2O_4$, and $Zn_{0.2}Mn_{0.8}Fe_2O_4$). Direct effect of exchange coupling is observed by comparison of physical properties of core/shell MNS with their single phase counterparts of the same size. Due to exchange coupling, higher magnetic susceptibility and anisotropy are observed in core/shell MNS compared to the single phase counterparts. As a result, r_2 relaxivity is doubled in core/shell MNS, resulting in values of up to 684 $mM^{-1}s^{-1}$, 7 times higher than FDA approved T_2 contrast agent Ferumoxtran. A specific absorption rate of up to 827 W/g is obtained from core/shell MNS, which is almost 9 times higher than conventional ferrite based MNS. Our findings present exchange coupling as an alternative approach to improve theranostic properties of biocompatible and soft magnetic ferrite based MNS. Due to their biocompatibility and excellent theranostic properties, exchange-coupled core/shell MNS show excellent potential in diagnostic imaging and drug delivery applications.

ASSOCIATED CONTENT

ⓢ Supporting Information

The Supporting Information is available free of charge on the ACS Publications website at DOI: 10.1021/acsami.8b09346.

> STEM image and low loss EELS line scan of Fe_3O_4/$MnFe_2O_4$ MNS (Figure S1); M−H and B−H loops of Fe_3O_4, $MnFe_2O_4$, and $Zn_{0.2}Mn_{0.8}Fe_2O_4$ samples at RT and 10 K (Figure S2); B−H loops of set 1 (Fe_3O_4, Fe_3O_4/$MnFe_2O_4$, Fe_3O_4/$Zn_{0.2}Mn_{0.8}Fe_2O_4$) and set 2 (Fe_3O_4, $MnFe_2O_4$/Fe_3O_4, $Zn_{0.2}Mn_{0.8}Fe_2O_4$/Fe_3O_4) samples at RT (Figure S3) (PDF)

AUTHOR INFORMATION

Corresponding Author

*E-mail: v-dravid@northwestern.edu.

ORCID Ⓞ

Vikas Nandwana: 0000-0002-7088-8813
Vinayak P. Dravid: 0000-0002-6007-3063

Notes

The authors declare no competing financial interest.

ACKNOWLEDGMENTS

REFERENCES

(1) Kneller, E. F.; Hawig, R. The Exchange-Spring Magnet - a New Material Principle for Permanent-Magnets. *IEEE Trans. Magn.* **1991**, *27*, 3588−3600.

(2) Fullerton, E. E.; Jiang, J. S.; Bader, S. D. Hard/Soft Magnetic Heterostructures: Model Exchange-Spring Magnets. *J. Magn. Magn. Mater.* **1999**, *200*, 392−404.

(3) Liu, F.; Hou, Y. L.; Gao, S. Exchange-Coupled Nanocomposites: Chemical Synthesis, Characterization and Applications. *Chem. Soc. Rev.* **2014**, *43*, 8098−8113.

(4) Zeng, H.; Li, J.; Wang, Z. L.; Liu, J. P.; Sun, S. H. Bimagnetic Core/Shell Fept/Fe3o4 Nanoparticles. *Nano Lett.* **2004**, *4*, 187−190.

(5) Zeng, H.; Li, J.; Liu, J. P.; Wang, Z. L.; Sun, S. H. Exchange-Coupled Nanocomposite Magnets by Nanoparticle Self-Assembly. *Nature* **2002**, *420*, 395−398.

(6) Nandwana, V.; Chaubey, G. S.; Yano, K.; Rong, C. B.; Liu, J. P. Bimagnetic Nanoparticles with Enhanced Exchange Coupling and Energy Products. *J. Appl. Phys.* **2009**, *105*, 014303.

(7) Chaubey, G. S.; Nandwana, V.; Poudyal, N.; Rong, C. B.; Liu, J. P. Synthesis and Characterization of Bimagnetic Bricklike Nanoparticles. *Chem. Mater.* **2008**, *20*, 475−478.

(8) Rong, C. B.; Nandwana, V.; Poudyal, N.; Liu, J. P.; Kozlov, M. E.; Baughman, R. H.; Ding, Y.; Wang, Z. L. Bulk Fept-Based Nanocomposite Magnets with Enhanced Exchange Coupling. *J. Appl. Phys.* **2007**, *102*, 023908.

(9) Tyagi, S.; Baskey, H. B.; Agarwala, R. C.; Agarwala, V.; Shami, T. C. Development of Hard/Soft Ferrite Nanocomposite for Enhanced Microwave Absorption. *Ceram. Int.* **2011**, *37*, 2631−2641.

(10) Lopez-Ortega, A.; Estrader, M.; Salazar-Alvarez, G.; Roca, A. G.; Nogues, J. Applications of Exchange Coupled Bi-Magnetic Hard/Soft and Soft/Hard Magnetic Core/Shell Nanoparticles. *Phys. Rep.* **2015**, *553*, 1−32.

(11) Feng, C.; Liu, X. G.; Or, S. W.; Ho, S. L. Exchange Coupling and Microwave Absorption in Core/Shell-Structured Hard/Soft Ferrite-Based Cofe2o4/Nife2o4 Nanocapsules. *AIP Adv.* **2017**, *7*, 056403.

(12) Wang, J. P.; Shen, W. K.; Bai, J. M. Exchange Coupled Composite Media for Perpendicular Magnetic Recording. *IEEE Trans. Magn.* **2005**, *41*, 3181−3186.

(13) Victora, R. H.; Shen, X. Composite Media for Perpendicular Magnetic Recording. *IEEE Trans. Magn.* **2005**, *41*, 537−542.

(14) Lee, J.-H.; Jang, J.-t.; Choi, J.-s.; Moon, S. H.; Noh, S.-h.; Kim, J.-w.; Kim, J.-G.; Kim, I.-S.; Park, K. I.; Cheon, J. Exchange-Coupled Magnetic Nanoparticles for Efficient Heat Induction. *Nat. Nanotechnol.* **2011**, *6*, 418−422.

(15) Song, Q.; Zhang, Z. J. Controlled Synthesis and Magnetic Properties of Bimagnetic Spinel Ferrite Cofe2o4 and Mnfe2o4 Nanocrystals with Core-Shell Architecture. *J. Am. Chem. Soc.* **2012**, *134*, 10182−10190.

(16) Lee, N.; Yoo, D.; Ling, D.; Cho, M. H.; Hyeon, T.; Cheon, J. Iron Oxide Based Nanoparticles for Multimodal Imaging and Magnetoresponsive Therapy. *Chem. Rev.* **2015**, *115*, 10637−10689.

(17) Shin, T. H.; Choi, Y.; Kim, S.; Cheon, J. Recent Advances in Magnetic Nanoparticle-Based Multi-Modal Imaging. *Chem. Soc. Rev.* **2015**, *44*, 4501−4516.

(18) Lee, N.; Hyeon, T. Designed Synthesis of Uniformly Sized Iron Oxide Nanoparticles for Efficient Magnetic Resonance Imaging Contrast Agents. *Chem. Soc. Rev.* **2012**, *41*, 2575−2589.

(19) Nandwana, V.; De, M.; Chu, S.; Jaiswal, M.; Rotz, M.; Meade, T. J.; Dravid, V. P. Nanotechnology-Based Precision Tools for the Detection and Treatment of Cancer. In *Cancer Treatment and Research*; Mirkin, C. A., Meade, T. J., Hurst Petrosko, S., Stegh, A. H., Eds.; Springer Nature: Cham, 2015; Vol. *166*, pp 51−83; DOI: 10.1007/978-3-319-16555-4_3

(20) Nandwana, V.; Ryoo, S. R.; Kanthala, S.; Kumar, A.; Sharma, A.; Castro, F. C.; Li, Y.; Hoffman, B.; Lim, S.; Dravid, V. P. Engineered Ferritin Nanocages as Natural Contrast Agents in Magnetic Resonance Imaging. *RSC Adv.* **2017**, *7*, 34892−34900.

(21) Reddy, L. H.; Arias, J. L.; Nicolas, J.; Couvreur, P. Magnetic Nanoparticles: Design and Characterization, Toxicity and Biocompatibility, Pharmaceutical and Biomedical Applications. *Chem. Rev.* **2012**, *112*, 5818−5878.

(22) Masala, O.; Hoffman, D.; Sundaram, N.; Page, K.; Proffen, T.; Lawes, G.; Seshadri, R. Preparation of Magnetic Spinel Ferrite Core/Shell Nanoparticles: Soft Ferrites on Hard Ferrites and Vice Versa. *Solid State Sci.* **2006**, *8*, 1015−1022.

(23) Zhang, Q.; Castellanos-Rubio, I.; Munshi, R.; Orue, I.; Pelaz, B.; Gries, K. I.; Parak, W. J.; del Pino, P.; Pralle, A. Model Driven Optimization of Magnetic Anisotropy of Exchange-Coupled Core-Shell Ferrite Nanoparticles for Maximal Hysteretic Loss. *Chem. Mater.* **2015**, *27*, 7380−7387.

(24) Ahmad, F.; Zhou, Y. Pitfalls and Challenges in Nanotoxicology: A Case of Cobalt Ferrite (Cofe2o4) Nanocomposites. *Chem. Res. Toxicol.* **2017**, *30*, 492−507.

(25) Ahmad, F.; Yao, H. Z.; Zhou, Y.; Liu, X. Y. Toxicity of Cobalt Ferrite (Cofe2o4) Nanobeads in Chlorella Vulgaris: Interaction, Adaptation and Oxidative Stress. *Chemosphere* **2015**, *139*, 479−485.

(26) Ahmad, F.; Liu, X. Y.; Zhou, Y.; Yao, H. Z. An in Vivo Evaluation of Acute Toxicity of Cobalt Ferrite (Cofe2o4) Nanoparticles in Larval-Embryo Zebrafish (Danio Rerio). *Aquat. Toxicol.* **2015**, *166*, 21−28.

(27) Mariani, V.; Ponti, J.; Giudetti, G.; Broggi, F.; Marmorato, P.; Gioria, S.; Franchini, F.; Rauscher, H.; Rossi, F. Online Monitoring of Cell Metabolism to Assess the Toxicity of Nanoparticles: The Case of Cobalt Ferrite. *Nanotoxicology* **2012**, *6*, 272−287.

(28) Porredon, C.; Ramos, D.; De Lapuente, J.; Camps, L.; Borras, M. Absorption, Biodistribution and Acute Toxicity of Cobalt Ferrite Np, Gold Np Hyaluronic Acid-Coated Gold Nanoparticles in Rats. *Toxicol. Lett.* **2010**, *196*, S280−S281.

(29) Schultz-Sikma, E. A.; Joshi, H. M.; Ma, Q.; MacRenaris, K. W.; Eckermann, A. L.; Dravid, V. P.; Meade, T. J. Probing the Chemical Stability of Mixed Ferrites: Implications for Magnetic Resonance Contrast Agent Design. *Chem. Mater.* **2011**, *23*, 2657−2664.

(30) Nandwana, V.; Ryoo, S. R.; Kanthala, S.; De, M.; Chou, S. S.; Prasad, P. V.; Dravid, V. P. Engineered Theranostic Magnetic Nanostructures: Role of Composition and Surface Coating on Magnetic Resonance Imaging Contrast and Thermal Activation. *ACS Appl. Mater. Interfaces* **2016**, *8*, 6953−6961.

(31) Nandwana, V.; Ryoo, S. R.; Kanthala, S.; McMahon, K. M.; Rink, J. S.; Li, Y.; Venkatraman, S. S.; Thaxton, C. S.; Dravid, V. P. High-Density Lipoprotein-Like Magnetic Nanostructures (Hdl-Mns): Theranostic Agents for Cardiovascular Disease. *Chem. Mater.* **2017**, *29*, 2276−2282.

(32) Nandwana, V.; Singh, A.; You, M. M.; Zhang, G.; Higham, J.; Zheng, T. S.; Li, Y.; Prasad, P. V.; Dravid, V. P. Magnetic Lipid Nanocapsules (Mlncs): Self-Assembled Lipid-Based Nanoconstruct for Non-Invasive Theranostic Applications. *J. Mater. Chem. B* **2018**, *6*, 1026−1034.

(33) Aquino, R.; Depeyrot, J.; Sousa, M. H.; Tourinho, F. A.; Dubois, E.; Perzynski, R. Magnetization Temperature Dependence and Freezing of Surface Spins in Magnetic Fluids Based on Ferrite Nanoparticles. *Phys. Rev. B: Condens. Matter Mater. Phys.* **2005**, *72*, 72.

(34) Zhao, G. P.; Wang, X. L. Nucleation, Pinning, and Coercivity in Magnetic Nanosystems: An Analytical Micromagnetic Approach. *Phys. Rev. B: Condens. Matter Mater. Phys.* **2006**, *74*, 012409.

(35) Zhao, G. P.; Zhao, M. G.; Lim, H. S.; Feng, Y. P.; Ong, C. K. From Nucleation to Coercivity. *Appl. Phys. Lett.* **2005**, *87*, 162513.

(36) Zhao, G. P.; Wang, X. L.; Feng, Y. P.; Huang, C. W. Coherent Rotation and Effective Anisotropy. *IEEE Trans. Magn.* **2007**, *43*, 2908−2910.

(37) Park, J.; Lee, E.; Hwang, N. M.; Kang, M. S.; Kim, S. C.; Hwang, Y.; Park, J. G.; Noh, H. J.; Kim, J. Y.; Park, J. H.; Hyeon, T. One-Nanometer-Scale Size-Controlled Synthesis of Monodisperse Magnetic Iron Oxide Nanoparticles. *Angew. Chem., Int. Ed.* **2005**, *44*, 2872−2877.

(38) Maaz, K.; Mumtaz, A.; Hasanain, S. K.; Ceylan, A. Synthesis and Magnetic Properties of Cobalt Ferrite (Cofe2o4) Nanoparticles Prepared by Wet Chemical Route. *J. Magn. Magn. Mater.* **2007**, *308*, 289−295.

(39) Liu, C.; Zhang, Z. J. Size-Dependent Superparamagnetic Properties of Mn Spinel Ferrite Nanoparticles Synthesized from Reverse Micelles. *Chem. Mater.* **2001**, *13*, 2092−2096.

(40) Nandwana, V.; Elkins, K. E.; Poudyal, N.; Chaubey, G. S.; Yano, K.; Liu, J. P. Size and Shape Control of Monodisperse Fept Nanoparticles. *J. Phys. Chem. C* **2007**, *111*, 4185−4189.

(41) Song, Q.; Zhang, Z. J. Correlation between Spin-Orbital Coupling and the Superparamagnetic Properties in Magnetite and Cobalt Ferrite Spinel Nanocrystals. *J. Phys. Chem. B* **2006**, *110*, 11205−11209.

(42) Skumryev, V.; Stoyanov, S.; Zhang, Y.; Hadjipanayis, G.; Givord, D.; Nogues, J. Beating the Superparamagnetic Limit with Exchange Bias. *Nature* **2003**, *423*, 850−853.

(43) Shiratsuchi, Y.; Yamamoto, M. Dominant Factor of Zero-Field-Cooled Magnetization in Discontinuous Fe Films. *Phys. Rev. B: Condens. Matter Mater. Phys.* **2007**, *76*, 144432.

(44) Morup, S.; Hansen, M. F.; Frandsen, C. Magnetic Interactions between Nanoparticles. *Beilstein J. Nanotechnol.* **2010**, *1*, 182−190.

(45) Koenig, S. H.; Kellar, K. E. Theory of 1/T-1 and 1/T-2 Nmrd Profiles of Solutions of Magnetic Nanoparticles. *Magn. Reson. Med.* **1995**, *34*, 227−233.

(46) Lee, J. H.; Huh, Y. M.; Jun, Y.; Seo, J.; Jang, J.; Song, H. T.; Kim, S.; Cho, E. J.; Yoon, H. G.; Suh, J. S.; Cheon, J. Artificially Engineered Magnetic Nanoparticles for Ultra-Sensitive Molecular Imaging. *Nat. Med.* **2007**, *13*, 95−99.

(47) Jang, J. T.; Nah, H.; Lee, J. H.; Moon, S. H.; Kim, M. G.; Cheon, J. Critical Enhancements of Mri Contrast and Hyperthermic Effects by Dopant-Controlled Magnetic Nanoparticles. *Angew. Chem., Int. Ed.* **2009**, *48*, 1234−1238.

(48) Simon, G. H.; Bauer, J.; Saborovski, O.; Fu, Y. J.; Corot, C.; Wendland, M. F.; Daldrup-Link, H. E. T1 and T2 Relaxivity of Intracellular and Extracellular Uspio at 1.5t and 3t Clinical Mr Scanning. *Eur. Radiol* **2006**, *16*, 738−745.

(49) Jordan, A.; Scholz, R.; Wust, P.; Fahling, H.; Felix, R. Magnetic Fluid Hyperthermia (Mfh): Cancer Treatment with Ac Magnetic Field Induced Excitation of Biocompatible Superparamagnetic Nanoparticles. *J. Magn. Magn. Mater.* **1999**, *201*, 413−419.

(50) Rosensweig, R. E. Heating Magnetic Fluid with Alternating Magnetic Field. *J. Magn. Magn. Mater.* **2002**, *252*, 370−374.

(51) Fannin, P. C.; Charles, S. W. The Study of a Ferrofluid Exhibiting Both Brownian and Neel Relaxation. *J. Phys. D: Appl. Phys.* **1989**, *22*, 187−191.

(52) Hergt, R.; Dutz, S. Magnetic Particle Hyperthermia-Biophysical Limitations of a Visionary Tumour Therapy. *J. Magn. Magn. Mater.* **2007**, *311*, 187−192.

(53) Carrey, J.; Mehdaoui, B.; Respaud, M. Simple Models for Dynamic Hysteresis Loop Calculations of Magnetic Single-Domain Nanoparticles: Application to Magnetic Hyperthermia Optimization (Vol 109, 083921, 2011). *J. Appl. Phys.* **2011**, *110*, 039902.

(54) Mehdaoui, B.; Tan, R. P.; Meffre, A.; Carrey, J.; Lachaize, S.; Chaudret, B.; Respaud, M. Increase of Magnetic Hyperthermia Efficiency Due to Dipolar Interactions in Low-Anisotropy Magnetic Nanoparticles: Theoretical and Experimental Results. *Phys. Rev. B: Condens. Matter Mater. Phys.* **2013**, *87*, 174419.

(55) Shaterabadi, Z.; Nabiyouni, G.; Soleymani, M. Optimal Size for Heating Efficiency of Superparamagnetic Dextran-Coated Magnetite Nanoparticles for Application in Magnetic Fluid Hyperthermia. *Phys. C* **2018**, *549*, 84−87.

(56) Mehdaoui, B.; Meffre, A.; Carrey, J.; Lachaize, S.; Lacroix, L. M.; Gougeon, M.; Chaudret, B.; Respaud, M. Optimal Size of Nanoparticles for Magnetic Hyperthermia: A Combined Theoretical and Experimental Study. *Adv. Funct. Mater.* **2011**, *21*, 4573−4581.

(57) Lacroix, L. M.; Malaki, R. B.; Carrey, J.; Lachaize, S.; Respaud, M.; Goya, G. F.; Chaudret, B. Magnetic Hyperthermia in Single-Domain Monodisperse Feco Nanoparticles: Evidences for Stoner-Wohlfarth Behavior and Large Losses. *J. Appl. Phys.* **2009**, *105*, 023911.

(58) Mehdaoui, B.; Meffre, A.; Lacroix, L. M.; Carrey, J.; Lachaize, S.; Gougeon, M.; Respaud, M.; Chaudret, B. Large Specific Absorption Rates in the Magnetic Hyperthermia Properties of Metallic Iron Nanocubes. *J. Magn. Magn. Mater.* **2010**, *322*, L49–L52.

(59) Saville, S. L.; Qi, B.; Baker, J.; Stone, R.; Camley, R. E.; Livesey, K. L.; Ye, L. F.; Crawford, T. M.; Mefford, O. T. The Formation of Linear Aggregates in Magnetic Hyperthermia: Implications on Specific Absorption Rate and Magnetic Anisotropy. *J. Colloid Interface Sci.* **2014**, *424*, 141–151.

(60) Nandwana, V.; Elkins, K. E.; Liu, J. P. Magnetic Hardening in Ultrafine Fept Nanoparticle Assembled Films. *Nanotechnology* **2005**, *16*, 2823–2826.

(61) Soares, J. M.; Cabral, F. A. O.; de Araujo, J. H.; Machado, F. L. A. Exchange-Spring Behavior in Nanopowders of Cofe2o4-Cofe2. *Appl. Phys. Lett.* **2011**, *98*, 072502.